Article:
Mostaed, E., Sikora-Jasinska, M., Wang, L. et al. (3 more authors) (2020) Tailoring the mechanical and degradation performance of Mg-2.0Zn-0.5Ca-0.4Mn alloy through microstructure design. JOM Journal of the Minerals, Metals and Materials Society, 72 (5). pp. 1880-1891. ISSN 1047-4838

https://doi.org/10.1007/s11837-020-04085-9

Tailoring the Mechanical and Degradation Performances of Mg-2.0Zn-0.5Ca-0.4Mn Alloy Through Microstructure Design

Ehsan Mostaed[1], Malgorzata Sikora-Jasinska[1], Lifei Wang[2], Ali Mostaed[3,4], Ian M. Reaney[3], Jaroslaw W. Drelich[1]

[1]Department of Materials Science and Engineering, Michigan Technological University, Houghton, MI 49931, USA

[2]College of Materials Science and Engineering, Taiyuan University of Technology, Taiyuan 030024, China

[3]Department of Engineering Materials, University of Sheffield, Sheffield, S1 3JD, UK

[4]Department of Materials, University of Oxford, Oxford, OX1 3PH, UK

Abstract

A novel Mg-2.0Zn-0.5Ca-0.4Mn alloy has been formulated and processed through melt spinning and hot extrusion to enhance its mechanical and degradation properties. Microstructural characterization of rapidly solidified alloy ribbons consolidated by extrusion revealed a fine and fully recrystallized microstructure with average size of 4 μm. The conventionally extruded alloy consisted of several course second-phase strips as coarse as 100 μm, while the extrusion-consolidated ribbons were devoid of any second phases larger than 100 nm. Rapid solidification followed by extrusion processing resulted in significantly randomized texture where the majority of the basal planes were tilted toward transverse and extrusion directions. Such a weak texture resulted in higher activity of basal planes and thereby considerably improved the fracture elongation from 4% to 19%, while retaining relatively high tensile strength of 294 MPa. In addition to high strength and ductility due to the reduced activity of deformation twining during compression, the extrusion-consolidated alloy ribbons showed lower yielding asymmetric ratio than that measured for the conventionally extruded alloy (1.25 versus 1.61). Electrochemical measurements and immersion tests indicated that application of rapid solidification followed by extrusion remarkably reduced the corrosion rate from 2.49 mm/year to 0.37 mm/year due to recrystallization completion and suppression of coarse second-phase formation.

Keywords: Mg alloy; biodegradable; Melt spinning; Dynamic precipitation; Corrosion

1. Introduction

Magnesium (Mg) alloys have received increasing attention as potential metallic materials for biodegradable orthopedic applications owing to their excellent biocompatibility, low density, and Young's modulus close to that of bone [1]. However, current Mg alloys degrade rapidly at the initial stage of implantation, causing excessive release of degradation products. In particular, the release of hydrogen (if the corrosion occurs quickly) can create gas pockets that might delay tissue healing at the implantation site, which results in necrosis [2]. Moreover, the rapid corrosion process of Mg alloys is accompanied by the release of a large amount of hydrogen gas, which can delay bone healing and even result in gas embolism [3]. Because of concerns regarding initial strength and rapid degradation, Mg alloys have been used primarily in non-loadbearing applications, including for screws used in surgical correction of hallux rigidus [4]. Therefore, it is of paramount importance to design Mg alloy implants with appropriate mechanical and corrosion behavior. Alloying Mg with rare-earth elements (REEs) results in increased mechanical properties and reduced degradation times [5]. However, alongside the high cost and natural

resource scarcity of REEs, there is a lack of consensus on their safe dosage; therefore, long-term clinical studies are required to provide appropriate feedback [6]. Hence, moving toward Mg alloys consisting of nutrient and osteoinductive elements with improved mechanical and degradation properties is of great interest for orthopedic applications. This confines the alloying element selection window to a few elements including zinc (Zn), calcium (Ca), and strontium (Sr).

Thus far, among the many Mg alloys explored as orthopedic implant materials, the Mg-Zn-Ca alloy system has attracted extensive attention, as both Zn and Ca are the most nutritionally essential elements in the human body [7, 8]. From the mechanical properties point of view, Zn shows relatively high solubility in Mg (about 6.2 wt.% at 325°C in equilibrium state) and thus can effectively improve the mechanical properties of Mg through the solid-solution strengthening and age-hardening mechanisms [9]. On the other hand, considering the low solubility of Ca in Mg (about 0.7 wt.% at 518°C in equilibrium state), addition of Ca results in marked grain refinement during solidification due to formation of Mg_2Ca and $Ca_2Mg_6Zn_3$ intermetallics [1]. Formation of these intermetallics promotes dynamic recrystallization during the thermomechanical processing through the particle stimulated nucleation mechanism and, as a consequence, enhances the strength and toughness of Mg alloys [10, 11]. Previous studies have reported that eutectic (α-Mg + $Ca_2Mg_6Zn_3$) phase forms in Mg–Zn–Ca alloys when the Zn/Ca atomic ratio is greater than 1.2 while eutectic (α-Mg + $Ca_2Mg_6Zn_3$ + Mg_2Ca) phase appears when this ratio is less than 1.2 [12]. The electrochemical corrosion potential order for the aforementioned phases is as follows: Mg_2Ca < α-Mg < $Ca_2Mg_6Zn_3$, thus in alloys contacting both Ca-containing phases, Mg_2Ca preferentially dissolves to α-Mg whereas α-Mg and Mg_2Ca preferentially dissolve to $Ca_2Mg_6Zn_3$ [13]. The corrosion of Mg alloys is mainly governed by galvanic coupling [14], thus the presence of secondary phases with different corrosion potentials compared with the Mg matrix remarkably accelerates the corrosion behavior. The microstructure of Mg-Zn-Ca alloys is heterogeneous even after hot processing, as the formation of coarse $Ca_2Mg_6Zn_3$ stringers elongated toward the processing direction is inevitable [11]. This accelerates the corrosion rate of these alloys by promoting the galvanic coupling between secondary phases and the α-Mg matrix. Accordingly, achieving high mechanical strength, which is possible by increasing the Zn and Ca contents, is always accompanied by deterioration of the corrosion properties. For this reason, this alloy system is inferior to REE-containing alloys, as it fails to simultaneously satisfy the mechanical and corrosion requirements.

An ideal biodegradable Mg implant should be devoid of coarse secondary phases. Previous studies have demonstrated that second-phase refinement down to the submicron regime can drastically improves the corrosion resistance and its uniformity, while remarkably enhancing the mechanical strength through promotion of particle dispersion strengthening [15, 16]. A novel experimental methodology for production of degradable REE-free Mg alloys with tailored mechanical and degradation behaviour without changing the alloy's elemental composition is introduced herein. In the present work, Mg-2.0Zn-0.5Ca (in wt.%) with trace (0.4 wt.%) addition of Mn was selected. Mn is recognized as a grain refiner and promotes grain refinement strengthening. Accordingly, the microstructure of the Mg-2.0Zn-0.5Ca-0.4Mn alloy was engineered by applying rapid solidification followed by hot extrusion, then its microstructural, mechanical, and corrosion properties were evaluated and compared with those of the conventionally extruded alloy.

2. Experimental Procedures

2.1.Materials and Methods

Pure Mg (99.9%), Zn (99.99%), Mn (99.93%) and Mg-30wt.% Ca master alloy were used for production of the alloy in this work. The alloy was cast at 710°C using permanent mold casting in an electric resistance furnace. The melting process was carried out under a protective atmosphere of CO_2 + SF_6. The melt was poured into a steel mold, with diameter of 40 mm. The alloy ingot was homogenized at 350°C for 12 h then extruded at 350°C with an extrusion ratio of 16:1 to form cylindrical rods. The alloy ingot was remelted in a vacuum induction furnace at 750°C under argon atmosphere. The melt was then ejected onto a copper wheel rotating at a speed of 1500 RPM and rapidly solidified to ribbons with thickness and width of approximately 50 µm and 2 mm, respectively. The alloy ribbons were compacted and extruded at 400°C with an extrusion ratio and speed of 10:1 and 0.3 mm s^{-1}, respectively.

2.2.Microstructural Analysis

All the investigated samples were cut to longitudinal sections. The samples were ground and polished following standard metallographic procedures. Microstructure was observed by scanning electron microscopy (SEM, XL 40; Philips). The macrotexture of the alloys was evaluated by x-ray diffraction (XRD) analysis (X'Pert Pro MRD; PANalytical) using Cu K_α radiation. Transmission electron microscopy (TEM) samples were prepared using standard routes, i.e. grinding and polishing the specimens to < 40 µm followed by ion beam milling using a GATAN precision ion polishing system II (PIPSII) to electron transparency. Ion beam milling was performed at liquid nitrogen temperature using Ar^+ ions, initially at 5 keV followed by final milling at 1 keV. TEM data were obtained using a JEOL JEM F200 transmission electron microscope operating at 200 kV.

2.3.Characterization of Mechanical Properties

The mechanical properties of the conventionally extruded (Ex) and extrusion-consolidated ribbon (RS+Ex) alloys were evaluated by tensile testing according to ASTM E8-04 specification [17]. Tensile specimens with their long axis along the extrusion direction were machined from the extruded billets with a gage length of 12 mm and diameter of 4 mm. Tensile testing on the extruded rods was performed at an initial strain rate of $1.8\times10^{-3}s^{-1}$. Compression tests were carried out at a strain rate of 1.8×10^{-3} s^{-1} on cylindrical specimens with diameter of 6 mm and height of 12 mm according to ASTM E9-09 specification [18]. The tensile and compression tests were carried out in triplicate for each condition.

2.4.Degradation Behavior

The corrosion behavior of the Ex and RS+Ex alloys was studied in Hanks' balanced salt solution (HBSS) supplemented with 0.35g $NaHCO_3$/L. The pH of the solution was adjusted to 7.4 using 1 M NaOH or HCl. Open-circuit potential (OCP), electrochemical impedance spectroscopy (EIS), and potentiodynamic polarization tests were carried out to study the corrosion behavior of the alloys. The potentiodynamic test was performed using a conventional three-electrode cell with a platinum counter-electrode of 1 cm^2 in surface area, a saturated calomel reference electrode, and the prepared Mg-based working electrode. A scan rate of 0.166 mV/s, with an applied potential range of 1 V was used. The experiments were carried out in an aerated environment at 37 ± 1°C. The electrodes were connected to a potentiostat and monitored using VersaStudio® software. For static immersion tests, alloy discs with 0.6 cm^2 exposed surface area were immersed for 7 days in Hanks' solution. Prior to immersion, the specimens were degreased ultrasonically in acetone for 5 min then dried. The whole volume of solution was changed every 2 days to keep the pH value close to 7.4. The containers were stored in a controlled temperature (T = 37 ± 1°C). The immersion tests were performed to evaluate the degradation progress and uniformity.

3. Results and Discussion

3.1.Microstructural Characterization

Figure 1 shows the microstructure of the as-cast Mg-2.0Zn-0.5Ca-0.4Mn alloy. The as-cast microstructure consisted of equiaxial α-Mg grains (average size about 50 μm) and secondary phases appearing in the form of fine spherical particles within the grain interiors and strips distributed at grain boundaries. Energy-dispersive spectroscopy (EDS) elemental maps (Fig. 1b) obtained from the area shown in the inset of Fig. 1a clearly revealed that the secondary phases were composed of Zn and Ca. As mentioned in the "Introduction", $Ca_2Mg_6Zn_3$ intermetallic forms in Mg-Zn-Ca alloys when the Zn/Ca atomic ratio exceeds 1.2 [12]. Hence, the secondary phase particles in the cast alloy are $Ca_2Mg_6Zn_3$. Mn was not detected in the EDS elemental maps as its content (0.4 wt.%) is below the detection limit of EDS in conventional SEM. According to the equilibrium Mg-Mn phase diagram, Mn does not react with Mg [19], thus, the trace addition of Mn in the Mg-Zn-Ca alloys remains in the form of pure α-Mn particles in the microstructure [20].

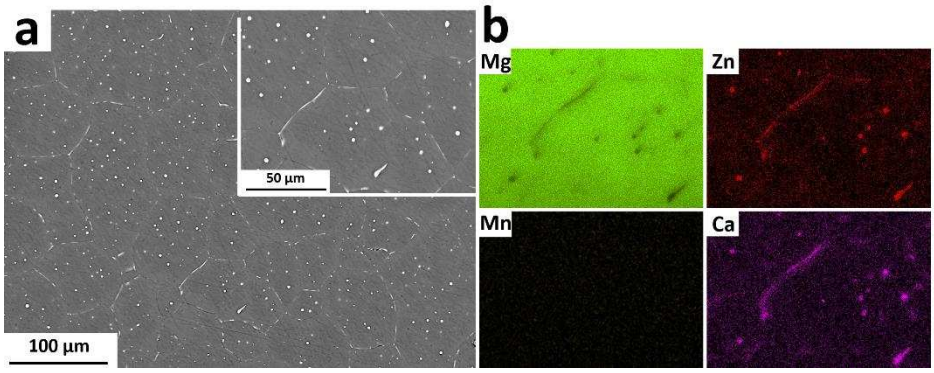

Fig. 1. (a) Backscattered SEM micrograph of as-cast material and (b) corresponding EDS elemental map in region displayed in inset.

Figure 2a presents a backscattered SEM image of the rapidly solidified (RS) ribbon cross section. The cross-sectional microstructure consisted of two distinct regions, marked by "*A*" and "*B*" in Fig. 2a. Region *A*, which was next to the wheel surface, had a thickness of ~3 μm and featured equiaxial fine grain structure with an average size of ~1.1 μm. Such remarkably fine grain structure is due to the high cooling rate at the Cu wheel surface. In the second region marked by "*B*" in Fig. 2a, the grains gradually evolved into columnar structure and extended to the free surface along the thermal gradient direction, which was nearly perpendicular to the wheel contact surface. Furthermore, Fig. 2a shows that the melt spun ribbon, alongside considerably refined grains, featured a microstructure without any secondary phases, implying that all the alloying elements were trapped in the Mg matrix. The presence of nanosized moiré fringes in the high-resolution TEM image of this alloy (e.g. Fig. 2b) indicates the presence of local strain inside the Mg grains. This means that the concentration of the elements varies within the alloy's grains due to local supersaturation of alloying elements in Mg. The highlighted areas could serve as nucleation sites for dynamic precipitation during subsequent thermomechanical processing.

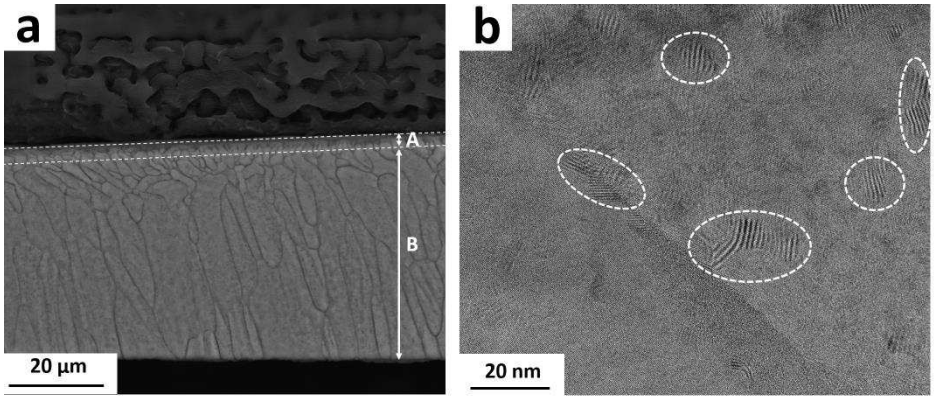

Fig. 2. (a) SEM and (b) high resolution TEM micrographs of RS ribbon alloy.

Figure 3a and b shows the microstructure of the Mg-2.0Zn-0.5Ca-0.4Mn alloy ingot after conventional extrusion (Ex) processing at two different magnifications. These micrographs show that extrusion resulted in the formation of a bimodal microstructure in the Mg-2.0Zn-0.5Ca-0.4Mn alloy with large deformed grains surrounded by extremely fine dynamically recrystallized (DRXed) grains with an average size of about 0.9 µm. Relatively coarse strings of $Ca_2Mg_6Zn_3$ particles in the range of 10 µm to 50 µm were heterogeneously distributed along the extrusion direction (white stringers in Fig. 2a). Figure 2b shows that DRXed grains nucleated in the vicinity of preexisting grain boundaries and on the deformation twins via grain boundary and twin-induced nucleation mechanisms, respectively.

Figure 3c and d displays the microstructure of the RS+Ex alloy. It can be seen that the melt-spun ribbons were perfectly bonded during extrusion: i.e. Ex resulted in full compaction of the RS ribbons without any evident porosities/voids. Indeed, the combined action of heat and compaction during hot extrusion led to the achievement of full densification of the melt-spun alloy ribbons. Moreover, interestingly, Fig. 3a and b reveals that the RS+Ex processed alloy featured a fully recrystallized equiaxial fine-grained structure with a size of ~4 µm. Indeed, no preferential elongation of the grains (deformed grains) could be seen in the RS+Ex alloy, which can be ascribed to the well distributed solute atoms in the matrix, promoting DRX uniformly throughout the matrix. Note that no fine and fully recrystallized microstructure for the Mg-Zn-Ca-based alloy system has been reported in literature so far. In addition to a fine and homogeneous grain structure, Fig. 3d indicates that the course $Ca_2Mg_6Zn_3$ particles observed in the Ex alloy were replaced with remarkably fine thermomechanically-induced precipitates with size below 1 µm (marked by white arrows). Such an engineered microstructure lacking coarse secondary phases has not been reported in Mg-Zn-Ca-based alloys and results in unprecedented mechanical and corrosion properties as discussed below.

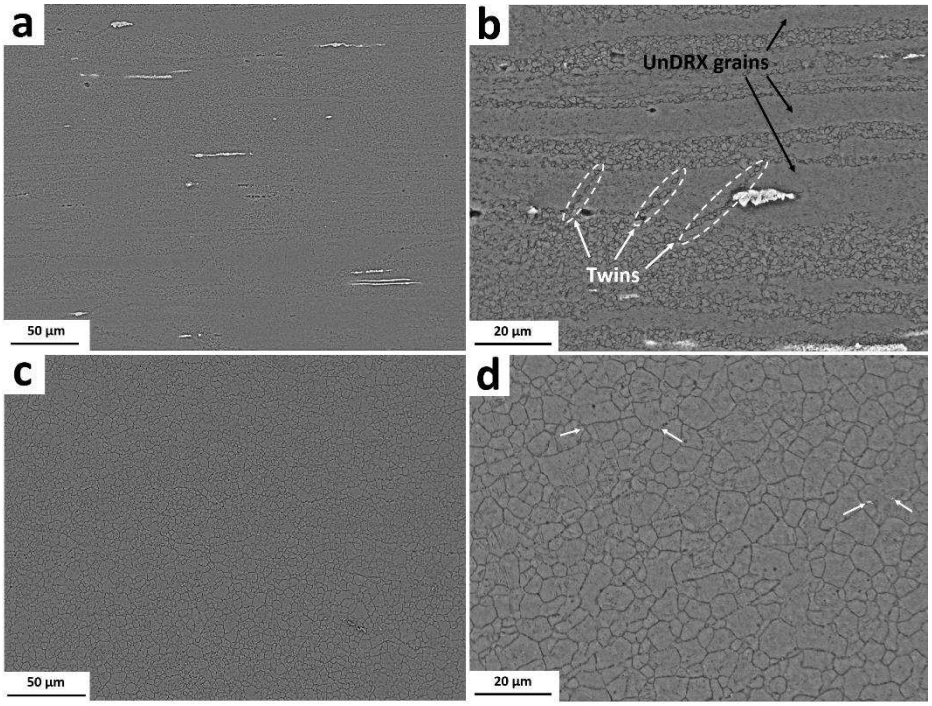

Fig. 3. Microstructures of alloy processed by (a, b) Ex and (c, d) RS+Ex.

Figure 4 shows bright-field scanning TEM (STEM) images as well as EDX elemental maps obtained from the DRXed area of the Ex alloy. Alongside the $Ca_2Mg_6Zn_3$ stringers observed in the Ex alloy (Fig. 3a and b), a large number of remarkably fine precipitates with nearly spherical morphology ranging from 50 nm to 100 nm formed through dynamic precipitation inside the grains and at grain boundaries (marked by white arrows in Fig. 4a). These intergranular precipitates can pin grain boundaries and hinder grain growth during hot extrusion. The EDS elemental map analysis confirmed that these precipitates are $Ca_2Mg_6Zn_3$ particles. Dynamic precipitation of $Ca_2Mg_6Zn_3$ phase has been previously reported in the Mg-Zn-Ca alloy system during hot deformation processes [11]. Figure 4b shows that in addition to the formation of strain-induced $Ca_2Mg_6Zn_3$ precipitates, extremely fine particles (indicated by red arrows) with size below 10 nm were dispersed within the grain interiors. These particles in some areas act as preferential nucleation sites for dynamic precipitation of $Ca_2Mg_6Zn_3$. EDS analysis demonstrated that these particles were pure Mn. Additionally, segregation of Ca and Zn atoms at grain boundaries can be clearly seen in Fig. 4b. Such co-segregation of Ca and Zn solutes to grain boundaries has been reported to exert a dragging effect on grain boundary mobility by reducing the grain boundary energy, thereby, hindering the growth of recrystallized grains during the hot extrusion process [21].

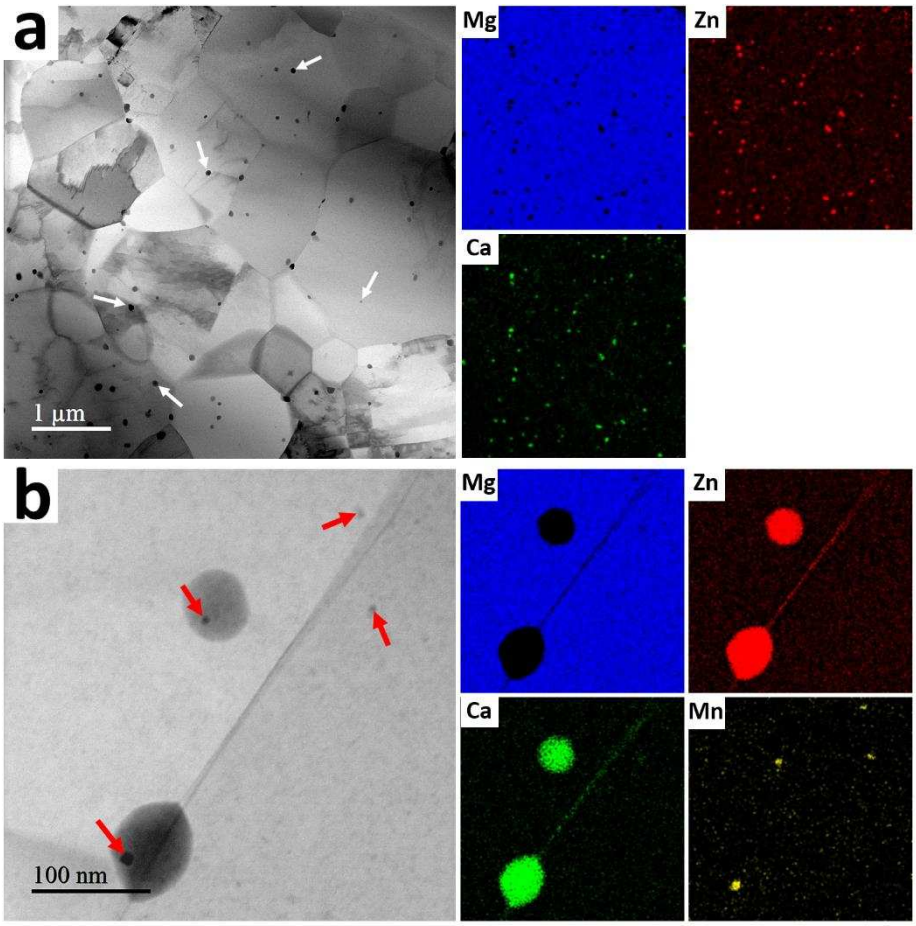

Fig. 4. Bright-field STEM images at (a) low and (b) high magnifications and corresponding EDX elemental maps obtain from Ex alloy.

For the alloy experiencing RS+Ex processing, the size and volume fraction of the thermomechanically-induced precipitates were smaller (Fig. 5a and b) than those in the Ex alloy. In the EDX elemental maps obtained from the RS+Ex alloy (Fig. 5), two types of precipitates were observed, one type containing Mg, Zn and Ca, i.e. $Ca_2Mg_6Zn_3$ (e.g. particles marked by circles in Fig. 5a), and another type containing Mg and Ca, i.e. Mg_2Ca (e.g. particles marked by squares in Fig. 5a). The EDX maps in Fig. 5 show that the intergranular precipitates were $Ca_2Mg_6Zn_3$ phase while the uniformly dispersed intragranular precipitates were Mg_2Ca phase in the RS+Ex alloy. Note that for this alloy composition (Mg-2Zn-0.5Ca-0.4Mn) Mg_2Ca phase is not thermodynamically favorable. However, we hypothesize that during Ex processing, the nanosized regions supersaturated in alloying elements observed in the RS alloy (Fig. 2b) transformed into refined spherical Mg_2Ca precipitates with a wide range of sizes from 10 nm to 100 nm. As the diffusivity of Ca in α-Mg is significantly higher than that of Zn [22], formation of Mg_2Ca could occur prior to $Ca_2Mg_6Zn_3$. Surprisingly, Fig. 5a reveals that the large amount of Zn alloying element remained trapped in the Mg matrix, emphasizing that the RS+Ex alloy is strongly vulnerable to age hardening. This could increase the fraction of nanosized Zn-rich precipitates and thus result in further improvement of mechanical properties. In other words, the mechanical properties of the RS+Ex alloy could be tuned to a large extent by engineering the fraction of precipitates via post age hardening. Similar to the Ex alloy, Mn was found in the form of markedly small particles within α-Mg grains, stimulating the nucleation of the second phases (Fig. 5b).

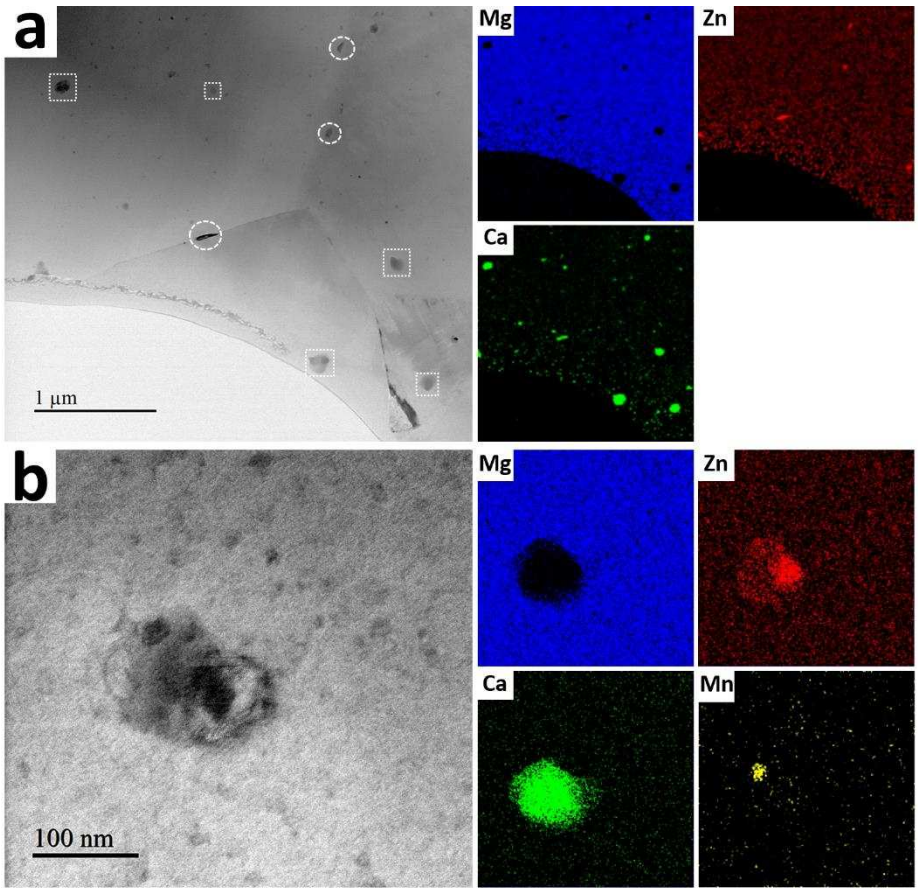

Fig. 5. Bright-field STEM images at (a) low and (b) high magnification and corresponding EDX elemental maps for RS+Ex alloy

3.2.Texture Analysis

Figure 5 depicts the results of macro-texture analysis on longitudinal sections of the Ex and RS+Ex alloys. The Ex alloy showed a rather weak basal texture with a maximum texture intensity of 6.6, where the basal planes were slightly tilted toward the transversal direction (TD), although the major texture component still exhibited the basal planes parallel to the extrusion direction (ED) (Fig. 5a). This is a typical texture of Mg-Zn-Ca alloys being similar to those of REE-containing alloys [23]. Interestingly, Fig. 6b shows that when the alloy was subjected to RS+Ex, a large number of basal planes were rotated about the normal direction (ND) toward the TD, developing a markedly weaker texture with a large distribution of basal planes. Zeng et al. [21] reported that DRXed grains exhibit weak basal texture in Mg-Zn-Ca alloys due to the Ca and Zn solute dragging effects on grain boundaries, which prevent grain growth on DRXed nuclei with preferential orientation, while the deformed grains are strongly textured. It is therefore suggested that in RS+Ex alloy due to the occurrence of complete recrystallization no strongly textured grains remained, thus, the overall texture was drastically weak. Indeed, the application of RS+Ex processing boosted the texture-randomizing effect and thereby, significantly decreased the texture intensity of the alloy from 6.6 to 3.5. The mechanical properties of Mg alloys are strongly dictated by their texture as it impacts on the activity of different deformation modes [16, 24]. Room temperature deformation of Mg alloys is mainly dominated by (0002) $<11\bar{2}0>$ basal slip since its critical resolved shear stress (CRSS) is far below those of the non-basal slip systems [25]. The newly developed texture in the RS+Ex alloy, due to the large distribution of grains having c-axis rotated toward TD and ED, provides

a high value of basal slip Schmid factor and thereby, significantly enhances the activity of basal slip during tension when the load is applied parallel to the ED [26, 27].

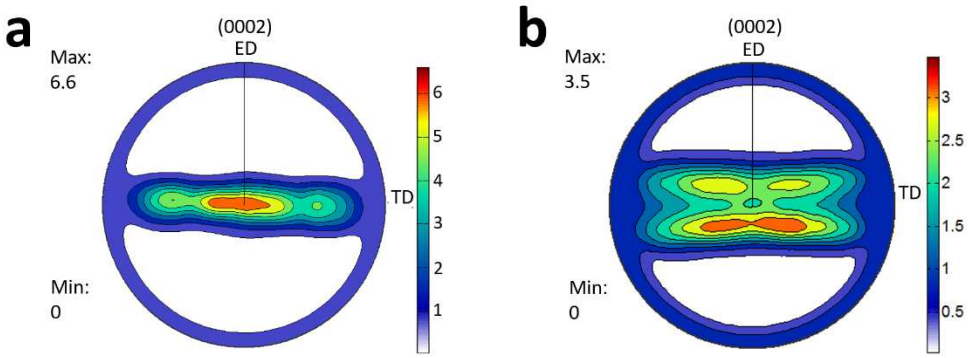

Fig. 6. (0002) pole figures for Ex and RS+Ex alloys.

3.3.Mechanical properties

The tensile and compressive stress versus strain curves for the Ex and RS+Ex alloys are presented in Fig. 7a and b. The 0.2% proof stress in tension (TYS) and compression (CYS), ultimate tensile strength (UTS), tensile fracture elongation (A) and yielding asymmetric ratio (represented by the ratio of tensile to compression yield strength) derived from Fig. 7 are summarized in Table I. In comparison with the RS+Ex alloy, the Ex alloy exhibited higher TYS (~40 MPa) and UTS (~10 MPa) but much lower fracture elongation (~4%). The higher strength of the Ex alloy is related to its bimodal microstructure which promotes various strengthening mechanisms. As shown in Fig. 4a and b, the Ex alloy consisted of submicron DRXed grains along with a large number of deformed grains (high density of dislocations), which boost the grain boundary strengthening and strain hardening mechanisms, respectively. Moreover, since the tensile direction is parallel to the ED, the unidirectional distribution of the $Ca_2Mg_6Zn_3$ strips contributes to the improvement of the tensile strength of this alloy. Eventually, the presence of these dynamically precipitated $Ca_2Mg_6Zn_3$ particles in the DRXed regions enhances the mechanical strength through promotion of the precipitation hardening mechanism. However, this alloy exhibited lower elongation due to its inhomogeneous microstructure (Fig. 3a and b) containing a large number of unDRXed grains (i.e. deformed grains) with high dislocation density which minimize the accommodation of large deformation. Moreover, previous studies have demonstrated that such deformed grains exhibit a very strong basal texture, which decreases the activity of basal slip during tensile deformation [11].

As presented in Fig. 6, RS+Ex processing created a markedly weak basal texture with a large angular distribution of basal planes toward TD and noticeable spread toward ED, resulting in an improvement of the basal Schmid factor value during tensile deformation. Higher activity of the dominant (0002) basal slip implies easier dislocation slip on the basal planes, which lowers the stress required for yielding during tensile deformation. Moreover, a large amount of deformation could be accommodated by increasing the activity of the basal slip, leading to a significant improvement of the fracture elongation (from 4% for the Ex alloy to 19% for the RS+Ex alloy). Note that, although the size of the DRXed grains in the Ex alloy was smaller than that in the RS+Ex one, its overall grain size (including DRXed and unDRXed grains) is considerably larger. Therefore, according to the Hall-Petch relationship, the RS+Ex alloy should exhibit higher TYS than the Ex alloy. However, the favorable basal texture orientation for the RS+Ex alloy counterbalances the grain refinement strengthening. Furthermore, for the RS+Ex alloy with the randomized texture, the number of mobile dislocations increases due to the facile basal

dislocation slip, thus, the accumulation of dislocations during plastic deformation leads to enhanced work hardening (Fig. 7a).

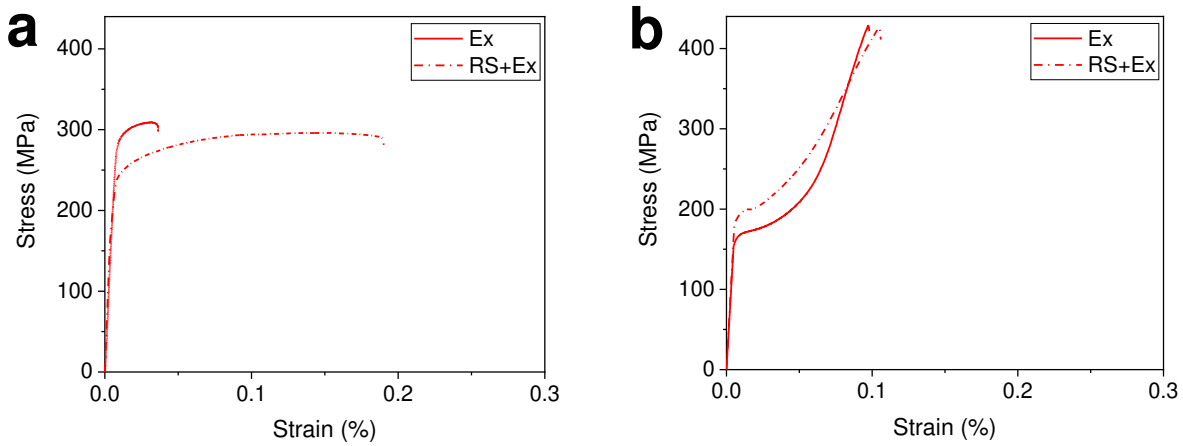

Fig. 7. (a) Tensile and (b) compressive stress-strain curves of Ex and RS+Ex alloys.

For the RS+Ex alloy, the thermomechanically-induced nanosized intergranular ($Ca_2Mg_6Zn_3$) and intragranular (Mg_2Ca) precipitates (Fig. 4) could effectively hinder dislocation movements during tensile deformation and result in an improved tensile strength of 294 MPa although this value is slightly lower than that measured for the Ex alloy (309 MPa). It should be emphasized that the RS+Ex alloy exhibited the best combination of strength, ductility and work hardening.

Table I. Tensile and compressive characteristics for Ex and RS+Ex alloys.

Material	YS (MPa)	UTS (MPa)	Young's Modulus (GPa)	A (%)	CYS (MPa)	UCS (MPa)	R
Ex	276 ± 6	309 ± 7	43 ± 1	4 ± 1	171 ± 5	429 ± 3	1.61
RS+Ex	237 ± 3	294 ± 7	42 ± 1	19 ± 3	190 ± 7	426 ± 5	1.25

In compression, however, the RS+Ex alloy showed higher CYS than its Ex counterpart (190 MPa versus 171 MPa). This is attributed to the considerably weak basal texture of the RS+Ex alloy, which reduces the activation of $\{10\bar{1}2\}$ $<10\bar{1}1>$ extension twining. It is well established that extension twining becomes activated when the compression load axis is parallel to the basal planes [28]. However, in the RS+Ex alloy, as shown in Fig. 6b, unlike the Ex alloy, due to the texture randomization, basal planes were rotated away from the ideal alignment for twinning activation which enhances the CRSS for twinning and thereby, suppresses the activation of extension twining [29]. Accordingly, texture modification is responsible for the enhanced CYS in the RS+Ex alloy. On the other hand, for the Ex alloy since the majority of the grains have texture favorable for generation of extension twining (Fig. 6a), the deformation is accommodated by dislocation slip and twinning, which results in lower CYS. In the Mg alloys, during compression testing, the twining-dominated plastic deformation was characterized by a concave-up stress-strain curve [30]. Figure 7b clearly shows that this feature is more distinct for the Ex alloy, confirming the lower twining activity in the RS+Ex alloy during compression. The low value of CYS led to a considerably high yielding asymmetric ratio of about 1.61 for the Ex alloy. The occurrence of tension-compression yield asymmetry is caused by easier plastic deformation via twinning during

compression than tension where slip is the dominant deformation mechanism. However, for the RS+Ex alloy, due to the suppression of deformation twinning resulting from the texture randomization, the aforementioned ratio decreased significantly to 1.25.

Tension–compression yield asymmetry restricts the use of Mg alloys as biomedical implants which are simultaneously subjected to tension and compression stresses (e.g. in bending or in axial tension–compression cycles). Accordingly, the more symmetric mechanical behavior of the RS+Ex alloy makes it a promising candidate for biodegradable implant applications.

In brief, a combination of dynamic precipitation of nanosized particles, grain refinement, and texture randomization was responsible for the concurrently improved strength and ductility as well as yield asymmetry alleviation in the RS+Ex alloy. In particular, the improved tensile strength is due to grain boundary strengthening and precipitation hardening, while the texture randomization is responsible for the high elongation and reduced yielding asymmetry.

3.4.Degradation Behavior

Potentiodynamic polarization testing was performed to determine the aspects that dictate the degradation rates of the Ex and RS+Ex alloys as it provides information regarding the anodic and cathodic reaction rates sustained by the investigated materials. Inspection of Fig. 8a reveals that the anodic kinetics of the RS+Ex alloy was significantly reduced relative to that of the conventionally processed counterpart. Indeed, the degradation rates for the RS+Ex samples calculated based on the current density and static immersion tests were obviously lower (0.37 mm/year and 0.12 mm/year, respectively) when compared with those for the Ex alloy (2.49 mm/year and 0.39 mm/year, respectively). Figure 8b shows the OCP time dependence for the Ex and RS+Ex samples. A sharp increase in the OCP could be observed in the first 72h of the degradation process for both the Ex and RS+Ex samples although the rate of increase varied. The rise in the OCP is attributed to the formation of degradation products with protective properties over time. However, a drop in the OCP was observed after 72h only for the Ex alloy. This reduction in the OCP could be due to the rupture of the protective layer and, as a consequence, localized corrosive attack.

The degradation behavior was further validated by EIS carried out regularly during continuous immersion in HBSS as a function of time. Nyquist and Bode diagrams obtained from both the Ex and RS+Ex alloys after various exposure times (1h, 24h, 72h, and 168h) are displayed in Fig. 8 c-e. The presence of capacitive loops at high/medium frequencies and an inductive loop at low frequencies in the Nyquist plots (Fig. 8c and e) indicates that different interfacial mechanisms are involved in the degradation process of the samples. The capacitive loop at high frequencies is associated with charge transfer and electrochemical double-layer/oxide-film effects while the capacitive loop at medium frequencies is associated with mass transport relaxation due to diffusion of Mg^{2+} ions through the degradation product layer [31]. The inductive loop at low frequencies observed only for the Ex alloys (Fig. 8c) is attributed to relaxation of coverage due to adsorption of Mg^{+} intermediates [32]. Comparing the Bode plots obtained from the alloys (Fig. 8d versus f), both the impedance and phase angle curves for the non-conventionally processed alloy showed a shift to lower frequency indicating a lower corrosion susceptibility for the RS+Ex sample. Furthermore, the impedance data reveal a large increase in the impedance of the RS+Ex sample after 168 h of exposure (from ~4000 $\Omega \cdot cm^2$ at 1h to ~15000 $\Omega \cdot cm^2$ at 168 h, Fig. 8f). However, for the Ex sample although there was an increase in the impedance in the early stage of the degradation process (for the first 24h), the impedance finally dropped to ~100 $\Omega \cdot cm^2$ after 168 h. The early rise in the corrosion resistance of both samples is caused by protective film formation due to the initial fast degradation rate leading to an increase in the local concentration of the Mg^{2+} and OH^{-} ions. The drop in the corrosion resistance of the Ex sample in the late stages could be due to severe localized corrosion

(arising from micro-galvanic coupling between the Mg matrix and cathodic secondary phases). The presence of localized corroded regions on the extruded alloy surface (Fig. 9a) confirms this suggestion regarding the occurrence of localized corrosion due to micro-galvanic coupling between the Mg matrix and cathodic secondary phases in this sample. Conversely, the RS+Ex alloy demonstrated a remarkably uniform degradation mode which can be attributed to its microstructural homogeneity (Fig. 9b), the absence of cathodic $Ca_2Mg_6Zn_3$ particles larger than 50 nm as well as their reduced fraction, and Mg matrix ennoblement (due to α-Mg saturation in Zn). Indeed, the low availability of hydrogen discharging cathodic sites on the surface of the RS+Ex alloy contributes to the lower exchange current density for hydrogen reduction on the homogenously oxidized surface [33]. In contrast, numerous, often large $Ca_2Mg_6Zn_3$ intermetallics exhibiting elevated cathodic activity in physiological conditions provoke severe deterioration of the Ex alloys' overall corrosion resistance and thus are the cause of drastic localized corrosion via microgalvanic coupling [34]. The rupture of the protective film on the extruded sample is evidenced by an increase in the low frequency inductive loop in Fig 8c. Protective layer dissolution and lateral pit growth are accompanied by increased electrolyte access to the interface of the conventionally processed sample leading to the reduction of the protective properties due to pit growth; this is evidenced by the decrease in the size of the high frequency loop after longer immersion times (Fig. 8c).

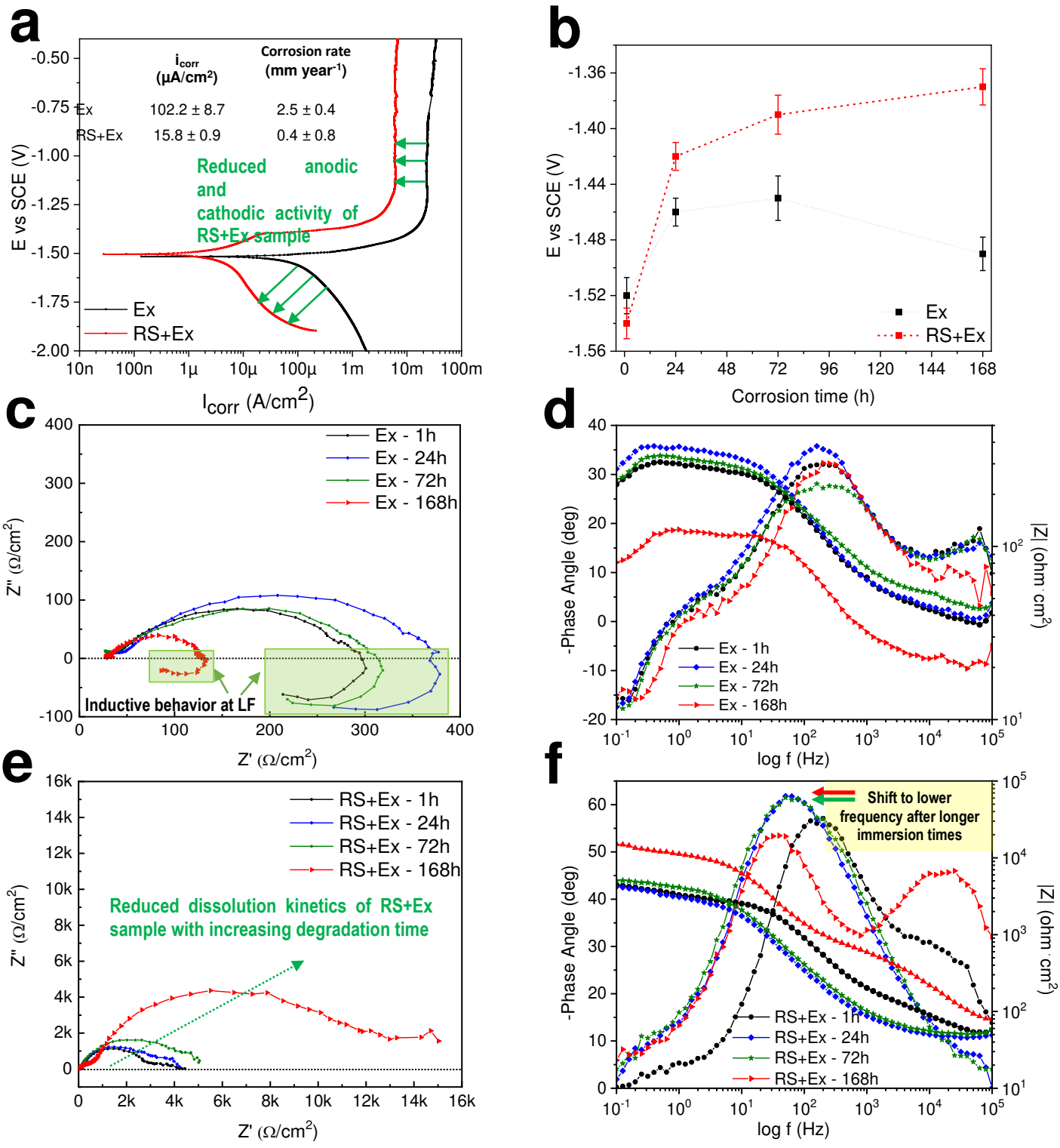
a
i_{corr} (μA/cm²)
Corrosion rate (mm year⁻¹)
Ex 102.2 ± 8.7 2.5 ± 0.4
RS+Ex 15.8 ± 0.9 0.4 ± 0.8
Reduced anodic and cathodic activity of RS+Ex sample
E vs SCE (V)
I_{corr} (A/cm²)
Ex
RS+Ex
b
E vs SCE (V)
Corrosion time (h)
Ex
RS+Ex
c
Ex - 1h
Ex - 24h
Ex - 72h
Ex - 168h
Inductive behavior at LF
Z'' (Ω/cm²)
Z' (Ω/cm²)
d
-Phase Angle (deg)
|Z| (ohm·cm²)
log f (Hz)
Ex - 1h
Ex - 24h
Ex - 72h
Ex - 168h
e
RS+Ex - 1h
RS+Ex - 24h
RS+Ex - 72h
RS+Ex - 168h
Reduced dissolution kinetics of RS+Ex sample with increasing degradation time
Z'' (Ω/cm²)
Z' (Ω/cm²)
f
Shift to lower frequency after longer immersion times
-Phase Angle (deg)
|Z| (ohm·cm²)
log f (Hz)
RS+Ex - 1h
RS+Ex - 24h
RS+Ex - 72h
RS+Ex - 168h

Fig. 8. (a) Potentiodynamic polarization curves and (b) OCP evolution for EX and RS+EX alloys. (c, e) Nyquist and (d, f) Bode plots for (c, d) Ex and (e, f) RS+EX samples after 1h, 24h, 72h and 168h of immersion in HBSS.

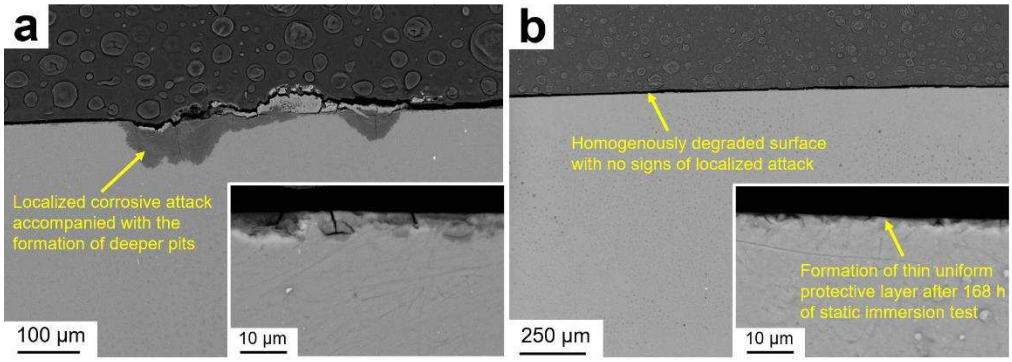

Fig. 9. Cross-sectional morphologies of degraded (a) Ex and (b) RS+Ex alloys.

4. Conclusions

A combination of rapid solidification and hot extrusion was exploited as a novel fabrication method to produce Mg-2.0Zn-0.5Ca-0.4Mn alloy with improved mechanical and corrosion properties through microstructural manipulation. Based on the results obtained, the following conclusions can be drawn:

- Rapidly solidified melt spun ribbons featured a single-phase structure in which all the alloying elements were trapped in the Mg matrix. The rapid solidification process caused the formation of nanosized regions supersaturated in the alloying elements in Mg which served as preferential nucleation sites for dynamic precipitation during the subsequent hot extrusion.
- Melt spun ribbons were successfully consolidated to a porosity-free bulk material via hot extrusion. The alloy ribbons consolidated by extrusion featured a fully recrystallized fine-grained structure with a size of ~4 µm. Moreover, application of RS+Ex suppressed the formation of coarse secondary phases and resulted in thermomechanically-induced nanosized precipitates, in the range of 10 nm to 100 nm, while a large amount of Zn remained dissolved in Mg.
- RS+Ex generated a random basal texture with a markedly reduced maximum intensity of 3.5, with the majority of basal planes rotated toward transverse and extrusion direction. This weak texture led to an increase in the basal slip Schmid factor and thereby significantly enhanced the activity of basal slip during tension when the load was applied parallel to the ED.
- The RS+Ex alloy exhibited enhanced tensile strength and fracture elongation of 294 MPa and 19 %, respectively, as well as reduced tension-compression yielding asymmetry (1.25). It was found that the improved strength could be attributed to promotion of the grain boundary strengthening and precipitation hardening mechanisms. However, texture weakening was responsible for high fracture elongation and reduced yielding asymmetry. In particular, the RS+Ex-induced texture was favorable for basal dislocation slip when the alloy was subjected to tension, resulting in larger accommodation of deformation by basal slip, while suppression of deformation twining during compression reduced the yielding asymmetry.
- The corrosion mode of the alloy varied with the microstructural features induced by the processing method. A more uniform corrosion pattern with a reduced rate was found for the RS+Ex alloy, replacing the predominant localized corrosion evident in the Ex alloy. Indeed, application of RS+Ex processing markedly decreased the corrosion rate from 2.5 mm/year to 0.4 mm/year mainly due to second phase refinement and microstructural homogenization.

The origin of the combined strengthening and enhanced corrosion resistance in the obtained alloy can be explained by the effective engineering of the solute nanostructures through careful control of the alloy chemistry and optimization of the thermal and mechanical processing route. This work provides a platform for further modification or control over the property profile of Mg–Zn-Ca-Mn alloys prepared through non-equilibrium processing methods and demonstrates the possibility of producing lightweight, high-strength and corrosion resistant alloys for potential use in diverse applications including as biodegradable implant materials.

5. Acknowledgements

The U.S. National Institute of Health – National Heart, Lung, and Blood Institute, Grant 1R01HL144739-01A1, and Michigan Tech College of Engineering, through Cross-Cutting Initiative funding, are acknowledged for funding this work. The authors also acknowledge the Engineering and Physical Sciences Research Council (EPSRC) grant EP/N032233/1 and the Henry Royce Institute for Advanced Materials, funded through EPSRC grants EP/R00661X/1 for JEOL JEM-F200 access at Royce@Sheffield. The authors also acknowledge the Applied Chemical and Morphological Analysis Laboratory (ACMAL) at Michigan Tech for use of instruments.

References

[1] Y.F. Zheng, X.N. Gu, F. Witte, Materials Science and Engineering: R: Reports 77 (2014) 1-34.
[2] X. Zhang, G. Yuan, J. Niu, P. Fu, W. Ding, J. Mech. Behav. Biomed. Mater. 9 (2012) 153-62.
[3] G. Song, Corrosion Science 49(4) (2007) 1696-1701.
[4] H. Windhagen, K. Radtke, A. Weizbauer, J. Diekmann, Y. Noll, U. Kreimeyer, R. Schavan, C. Stukenborg-Colsman, H. Waizy, Biomed. Eng. Online 12(62) (2013).
[5] C. Plaass, C. von Falck, S. Ettinger, L. Sonnow, F. Calderone, A. Weizbauer, J. Reifenrath, L. Claassen, H. Waizy, K. Daniilidis, C. Stukenborg-Colsman, H. Windhagen, J. Orthop. Sci. 23(2) (2018) 321-327.
[6] G. Pagano, M. Guida, F. Tommasi, R. Oral, Ecotoxicol. Environ. Saf. 115 (2015) 40-8.
[7] J. Ma, N. Zhao, D. Zhu, ACS Biomater Sci Eng 1(11) (2015) 1174-1182.
[8] Z. Li, X. Gu, S. Lou, Y. Zheng, Biomaterials 29(10) (2008) 1329-44.
[9] S. Zhang, X. Zhang, C. Zhao, J. Li, Y. Song, C. Xie, H. Tao, Y. Zhang, Y. He, Y. Jiang, Acta Biomater. 6(2) (2010) 626-640.
[10] H. Somekawa, T. Mukai, Materials Science and Engineering: A 459(1-2) (2007) 366-370.
[11] S.W. Xu, K. Oh-ishi, H. Sunohara, S. Kamado, Materials Science and Engineering: A 558 (2012) 356-365.
[12] T. V. Larionova, W.W. Park, B.S. You, Scripta Materialia 45(1) (2001) 7-12.
[13] D. Zander, N.A. Zumdick, Corrosion Science 93 (2015) 222-233.
[14] M. Esmaily, J.E. Svensson, S. Fajardo, N. Birbilis, G.S. Frankel, S. Virtanen, R. Arrabal, S. Thomas, L.G. Johansson, Progress in Materials Science 89 (2017) 92-193.
[15] G. Qiang, E. Mostaed, C. Zanella, Y. Zhentao, M. Vedani, Rare Metal Materials and Engineering 43(11) (2014) 2561-2566.
[16] E. Mostaed, M. Hashempour, A. Fabrizi, D. Dellasega, M. Bestetti, F. Bonollo, M. Vedani, J. Mech. Behav. Biomed. Mater. 37 (2014) 307-22.
[17] ASTM E8-04, 2004, Standard Test Methods for Tension Testing of Metallic Materials, Annual Book of ASTM Standards.
[18] ASTM E9-09, Annual book of ASTM standards, (2009).
[19] M.M. Avedesian, H. Baker, ASM International (1999).
[20] Y. Xin, T. Hu, P.K. Chu, Acta Biomater. 7(4) (2011) 1452-9.

[21] Z.R. Zeng, Y.M. Zhu, S.W. Xu, M.Z. Bian, C.H.J. Davies, N. Birbilis, J.F. Nie, Acta Materialia 105 (2016) 479-494.
[22] G. Levi, S. Avraham, A. Zilberov, M. Bamberger, Acta Materialia 54(2) (2006) 523-530.
[23] J. Bohlen, M.R. Nürnberg, J.W. Senn, D. Letzig, S.R. Agnew, Acta Materialia 55(6) (2007) 2101-2112.
[24] E. Mostaed, A. Fabrizi, D. Dellasega, F. Bonollo, M. Vedani, Materials Characterization 107 (2015) 70-78.
[25] R.E. Reed-Hill, W.D. Robertson, Acta Metallurgica 5(12) (1957) 728-737.
[26] X.-L. Nan, H.-Y. Wang, L. Zhang, J.-B. Li, Q.-C. Jiang, Scripta Materialia 67(5) (2012) 443-446.
[27] E. Mostaed, A. Fabrizi, D. Dellasega, F. Bonollo, M. Vedani, Journal of Alloys and Compounds 638 (2015) 267-276.
[28] S. Kleiner, P.J. Uggowitzer, Materials Science and Engineering: A 379(1-2) (2004) 258-263.
[29] M. A. Meyers, O. Vohringer, V.A. Lubarda, Acta Materialia 49(19) (2001) 4025–4039.
[30] F. Kabirian, A.S. Khan, T. Gnäupel-Herlod, Journal of Alloys and Compounds 673 (2016) 327-335.
[31] R. Rettig, S. Virtanen, J. Biomed. Mater. Res. A 85(1) (2008) 167-75.
[32] N. Pebere, C. Riera, F. Dabosi, Electrochimica Acta 35(2) (1990) 555-561.
[33] M. Ascencio, M. Pekguleryuz, S. Omanovic, Corrosion Science 87 (2014) 489-503.
[34] S.A. Abdel-Gawad, M.A. Shoeib, Surfaces and Interfaces 14 (2019) 108-116.